Al$_2$O$_3$/ZnO Heterostructure-Based Sensors for Volatile Organic Compounds in Safety Applications

Oleg Lupan,[1,2,3,*] David Santos-Carballal,[4,*] Nicolae Magariu,[2] Abhishek Kumar Mishra,[5]

Nicolai Ababii,[2] Helge Krüger,[1] Niklas Wolff,[6] Alexander Vahl,[7,*] Mani Teja Bodduluri,[8] Niklas

Kohlmann,[6] Lorenz Kienle,[6,*] Rainer Adelung,[1,*] Nora H de Leeuw,[4,9] Sandra Hansen,[1,*]

[1] *Department of Materials Science, Chair for Functional Nanomaterials, Faculty of Engineering, Christian-Albrechts Universität zu Kiel, Kiel, Kaiserstraße 2, D-24143 Kiel, Germany*
[2] *Center for Nanotechnology and Nanosensors, Department of Microelectronics and Biomedical Engineering, Faculty of Computers, Informatics and Microelectronics, Technical University of Moldova, 168 Stefan cel Mare str., MD-2004, Chisinau, Republic of Moldova*
[3] *Department of Physics, University of Central Florida, Orlando, Florida, FL 32816-2385, USA*
[4] *School of Chemistry, University of Leeds, Leeds LS2 9JT, United Kingdom*
[5] *Department of Physics, School of Engineering, University of Petroleum and Energy Studies (UPES), Energy Acres Building, Bidholi, Dehradun 248007, Uttrakhand, India*
[6] *Department of Materials Science, Chair for Synthesis and Real Structure, Faculty of Engineering, Christian-Albrechts Universität zu Kiel, Kiel, Kaiserstraße 2, D-24143 Kiel, Germany*
[7] *Department of Materials Science, Chair for Multicomponent Materials, Faculty of Engineering, Christian-Albrechts Universität zu Kiel, Kiel, Kaiserstraße 2, D-24143 Kiel, Germany*
[8] *Fraunhofer Institute for Silicon Technology (ISIT), Itzehoe, Fraunhoferstraße 1, D- 25524, Germany*
[9] *Department of Earth Sciences, Utrecht University, Princetonlaan 8a, 3584 CB Utrecht, The Netherlands*

[*]Corresponding authors:
Prof. Dr. O. Lupan, (ollu@tf.uni-kiel.de ; oleg.lupan@mib.utm.md)
Kiel University, Germany; Technical University of Moldova, Moldova; UCF, U.S.A.

Dr. David Santos-Carballal (d.santos-carballal@leeds.ac.uk)
University of Leeds, United Kingdom

Prof. Dr. L. Kienle, (lk@tf.uni-kiel.de)
Kiel University, Germany

Prof. Dr. R. Adelung, (ra@tf.uni-kiel.de)
Kiel University, Germany

Dr. A. Vahl, (alva@tf.uni-kiel.de)
Kiel University, Germany

Dr. S. Hansen, (sn@tf.uni-kiel.de)
Kiel University, Germany

ABSTRACT

Monitoring volatile organic compounds (VOCs) in harsh environments, especially for safety applications, is a growing field that requires specialized sensor structures. In this work, we demonstrate the sensing properties towards the most common VOCs of columnar Al_2O_3/ZnO heterolayer-based sensors. We have also developed an approach to tune the sensor selectivity by changing the thickness of the exposed amorphous Al_2O_3 layer from 5 to 18 nm. Columnar ZnO films are prepared by a chemical solution method, where the exposed surface is decorated with an Al_2O_3 nanolayer via thermal atomic layer deposition at 75 °C. We have investigated the structure and morphology, as well as vibrational, chemical, electronic, and sensor properties of the Al_2O_3/ZnO heterostructures. Transmission electron microscopy (TEM) studies show that the upper layers consist of amorphous Al_2O_3 films. The heterostructures showed selectivity to 2-propanol vapors only within the range of 12 - 15 nm thicknesses of Al_2O_3, with the highest response value of approximately 2000% reported for a thickness of 15 nm at the optimal working temperature of 350 °C.

Density functional theory (DFT) calculations of the Al_2O_3/ZnO($10\bar{1}0$) interface and its interaction with 2-propanol (2-C_3H_7OH), n-butanol (n-C_4H_9OH), ethanol (C_2H_5OH), and acetone (CH_3COCH_3), hydrogen (H_2) and ammonia (NH_3) show that the molecular affinity for the Al_2O_3/ZnO($10\bar{1}0$) interface decreases from 2-propanol (2-C_3H_7OH) ≈ n-butanol (n-C_4H_9OH) > ethanol (C_2H_5OH) > acetone (CH_3COCH_3) > hydrogen (H_2), which is consistent with our gas response experiments for the VOCs. Charge transfers between the surface and the adsorbates, and local densities of states of the interacting atoms, support the calculated strength of the molecular preferences. Our findings are highly important for the development of 2-propanol sensors and to our understanding of the effect of the heterojunction and the thickness of the top nanolayer on the gas response, which thus far has not been reported in the literature.

1. Introduction

Volatile organic compounds (VOCs), which originate from multiple sources such as household items, cooking appliances, paint, oil refineries, and vehicle exhaust emissions, are highly hazardous vapors that affect significantly human health and air quality in various industrial environments [1–4]. Despite having been investigated extensively over the past few years, the sensing properties towards VOCs need to be improved continuously to meet the most up-to-date requirements for specific applications and to withstand the harsh industrial environments, especially when using heterostructures or heterojunctions of two or more metal oxides [3–5]. The selective detection of low concentrations of VOCs is highly important to underpin the continuous monitoring of human health and for environmental safety [5]. Among the various types of materials available, the semiconducting – metal oxide-based chemo-resistive sensors are considered to be promising candidates for the detection of VOCs, [2,6] especially those comprising heterostructures/heterojunctions containing two or more different oxides, as these materials show excellent potential for their application in portable solid-state devices, due to their low cost, high efficiency, simple preparation method, and good stability [1–9]. In the context of real-world applications, the response parameter is influenced by several factors, including the morphology [10], microstructure, defects, and heterojunctions of the VOC sensors, as well as the relative humidity [6]. The response and selectivity performance of solid-state gas sensors can be improved further through control of their properties and, especially, by developing new multilayered or heterostructured oxides with a coating of Al$_2$O$_3$ nanofilms. These films provide an effective protective layer against harsh environments since they can withstand high temperatures and/or inaccessible environments [11–13].

3

A recently developed approach to improve the sensitivity of chemoresistive sensors towards common VOCs involves the preparation of mixed or heterostructured/multilayered nanomaterials, including copper oxide, zinc oxide, indium oxide, aluminum oxide, titanium oxide, and several other semiconducting metal oxides. The literature includes reports on the fabrication of new heterostructures of TiO_2/CuO [14], Al_2O_3/CuO [5], ZnO/In_2O_3 [15], Mn_3O_4/Fe_2O_3, and Mn_3O_4/ZnO [16], ZnO-SnO_2 [17] and their functionalization with metallic nanoparticles such as Pd, Ag, Pt and Au [14,18,19]. These multilayered heteromaterials have been used as sensor devices for the detection of hydrogen gas or volatile organic compounds, or in the production of solar cells [20], photodetectors [21], photocatalysts [15,22] and light-emitting diodes [23].

In this study, we investigate the response of the Al_2O_3/ZnO heterostructure to 2-propanol (2-C_3H_7OH), n-butanol (n-C_4H_9OH), ethanol (C_2H_5OH), acetone (CH_3COCH_3), molecular hydrogen (H_2) and ammonia (NH_3) vapors in low concentrations. In addition, DFT calculations were used to model the $Al_2O_3/ZnO(10\bar{1}0)$ interface and its interaction with the VOCs and molecular hydrogen (H_2). The adsorption energies and structures of the molecules at the interface are evaluated, whereas the charge transfers and electronic densities of states for the most favorable molecular binding modes are calculated to examine the selectivity and sensitivity of the developed heterostructured sensor.

2. Experimental Section

2.1. Synthesis of Al₂O₃/ZnO heterostructures

Columnar zinc oxide thin films were synthesized from chemical solutions (SCS) of zinc sulfate at 95 °C over quartz silica or glass substrates, where the nanocrystalline layers were produced following thermal annealing treatment. Details of the preparation procedure can be found in our previous works [24–27], whereas the cross-section of the columnar structure of these films has also been reported before [8]. Standard thermal treatment in an electrical furnace at 450, 550, and 650 °C

for 120 min was involved/used as a post-growth thermal treatment process, which improved essentially/significantly the crystallinity of the SCS deposited columnar ZnO layers [24,26,28,29].

Next, a coating of an Al_2O_3 nano-film was deposited on top of the columnar zinc oxide films/layers and ZnO nanowire model systems [30] using a thermal atomic layer deposition (ALD) method (Picosun's R200) at 75 °C, with different numbers of runs to control the thickness of the top nanolayer [5,31]. Picoflow^{TM} technology was involved/applied to achieve uniform nano-layer coating depositions on high-aspect-ratio structures, such as nanowire networks or materials with difficult morphologies, like interpenetrated column-based films. Trimethylaluminum (TMA) was used as the aluminum source, which was oxidized using H_2O after chemisorption. Alternating pulses with a duration of 0.2 s per pulse were applied to insert the precursors into the reactor chamber where the Al_2O_3 monolayers were grown. N_2 gas was involved/utilized to carry the precursors' vapors into the reaction prechamber and to get rid/eliminate the by-products from the reactor.

To study the thickness of the Al_2O_3 thin film coating deposited on the columnar ZnO films, we used a flame synthesis approach [30] to prepare a suitable model system consisting of ZnO nanowires, which were homogeneously coated using the ALD method with identical process parameters. Such nanowires are regarded as highly congruent systems that bypass the advanced sample preparation methods required for electron microscopy imaging.

Further, the Al_2O_3/ZnO thin film and nanowire heterostructures were thermally treated at 620 °C for 40 min in a furnace to improve the crystallinity and stability during the sensing measurements.

2.2. Structural, morphological, vibrational, chemical, and spectroscopic characterization of the Al_2O_3/ZnO heterostructures

The morphology of the Al_2O_3/ZnO heterostructures was measured using a Zeiss Ultraplus scanning electron microscope (SEM) at 7 kV. To study the reproducibility of the deposition

technique, the uniformity of the Al_2O_3 layers, and possible crystallization effects during the subsequent thermal annealing, we carried out transmission electron microscopy (TEM) experiments of Al_2O_3 -coated ZnO nanowires, as a model of columnar Al_2O_3/ZnO heterostructures, using a JEOL JEM2100 instrument equipped with a thermionic LaB_6 cathode operating at 200 kV. Energy-dispersive X-ray spectroscopy (EDXS) was conducted using an Oxford AztecEnergyTEM EDXS-System with an 80 mm^2 Silicon drift (SD) detector. The linescan data were low-pass filtered during counts to reduce the signal-to-noise ratio and enhance the X-ray patterns. The crystallographic structures were investigated using X-ray powder diffraction (XRD) with a Seifert 3000 unit operating with CuKα1 radiation (1.540598 Å) at 40 kV and 40 mA. MicroRaman experiments were measured using the 532 nm line from a laser as the excitation light source.

To find additional information on stoichiometry and chemical composition, we performed X-rays photoelectrons spectroscopy (XPS, Omicron Nano-Technology GmbH, Al-anode, 240W) on both columnar ZnO and Al_2O_3/ZnO thin film samples grown on quartz glass substrates. The software CasaXPS (version 2.3.16) was used to correct potential charging, by adjusting the main C-1s line of all experiments to 284.5 eV, which is the reference value of adventitious carbon [32,33].

2.3 Density functional theory calculations

Calculations based on the density functional theory (DFT) were realized/carried out using the generalized gradient approximation with the Perdue–Burke–Ernzerhof (PBE) [34] exchange-correlation functional and the projected augmented wave (PAW) [35,36] method, as implemented in the Vienna *ab initio* Simulation Package (VASP) [37–40]. The atomic positions and lattice constants of the ZnO bulk structure were optimized using the conjugate gradient method until the maximum residual force acting on each atom was less than 0.01 eV/Å, as in our earlier works [8,41–43], where the criterion for energy convergence was 10^{-5} eV/cell. Here, a cutoff of 520 eV was used for the kinetic energy of the plane waves, and Γ-centred $5 \times 5 \times 4$ and $5 \times 3 \times 1$ Monkhorst-Pack k points

meshes [44] were involved/used to simulate the bulk and $(10\bar{1}0)$ surface structures, respectively. The electronic partial occupancies were determined using the Gaussian smearing technique, which has been used previously to model the ZnO bulk, its $(10\bar{1}0)$ surface and the Al_2O_3/ZnO$(10\bar{1}0)$ interface [8,41,42]. Similar to earlier works [45,46], the termination of the $(10\bar{1}0)$ surface (**Figure S1**) with a surface energy of 1.12 J·m^{-2} was found to be the most stable. The $(10\bar{1}0)$ surface has two different types of cations, the most exposed surface Zn atoms form bonds to three oxygen atoms in the top layer, whereas the sub-surface Zn atoms are comparatively less exposed, as they form bonds with three oxygen atoms in the top layer and one oxygen atom in the second layer, as shown in **Figure S1**. The semi-empirical method of Grimme (D2) was included in our calculations to account for the long-range dispersion corrections [47]. Atomic charges were obtained using the Bader analysis [48,49].

To model the Al_2O_3/ZnO $(10\bar{1}0)$ interface, three Zn ions from the surface and sub-surface layers were replaced with two Al atoms in a 2×2 super-cell of the ZnO $(10\bar{1}0)$ surface. Here, the energies of different configurations were calculated and the most stable system was identified by replacing two sub-surface Zn atoms with Al atoms and removing one most exposed surface Zn atom nearby. After relaxation, it was noted that both substituted Al atoms coordinate four oxygen atoms with bond lengths varying from 1.751 Å to 1.861 Å, as demonstrated by our results shown in **Figure 1**.

3. Results and Discussion

3.1. Structural characterization of the Al₂O₃/ZnO heterostructures

As-deposited and annealed Al_2O_3/ZnO nanowire model structures were examined by TEM to determine the layer thickness for amorphous Al_2O_3 coatings targeting 3 to 18 nm, (3, 5, 7, 10, 12, 15, 18 nm – 30, 50, 70, 100, 120, 150, 180 deposition cycles, respectively), and their resistance to

crystallization upon annealing at 620 °C (**Figure 2**). The ZnO nanowires exhibit high crystallinity, which allows for the distinct identification of the interface between the amorphous and crystalline components of Al_2O_3 and ZnO and accurate measurements of the amorphous shell thickness. TEM and high-resolution micrographs are presented for representative Al_2O_3/ZnO heterostructures with 7 and 18 nm of Al_2O_3 in **Figure 2a,b** before and after thermal treatment at 620 °C for 40 minutes, showing the (0001) lattice planes of ZnO covered by the amorphous Al_2O_3 layer. Chemical analysis by an EDXS linescan recorded across one Al_2O_3/ZnO nanowire heterostructure (see **Figure 2c**) confirms the homogeneity of the aluminum oxide coating around the nanostructure. The HRTEM analysis as well as extended selected-area electron diffraction experiments (see **Figure 2d**) show crystallization resistance of the amorphous oxide at temperatures as high as 620 °C given the absence of reflections from a second nanocrystalline phase. Further, we observed no significant changes in the thickness or homogeneity of the layers after annealing. To determine the reliability of the ALD process targeting 3-18 nm of Al_2O_3, the measured shell thicknesses are statistically evaluated and compared against the ZnO nanowire diameter in **Figure 2e** and the targeted thickness in **Figure 2f**. As expected, the scatter plots demonstrate the little variation of Al_2O_3 thicknesses versus the ZnO diameter. Further, the scatter measurements are summarized in box plots showing the average layer thickness, the standard variation and the 25-75 percentile intervals (colored boxes), which attest to the reliability of the ALD process, even when targeting small thicknesses, concluding identical deposition characteristics on columnar ZnO thin films. For example, when targeting 3 or 7 nm, this results in an average deposited layer thicknesses of 2.9 ± 0.1 nm and 6.7 ± 0.5 nm, respectively.

X-ray diffraction (XRD) evaluation/analysis was performed to investigate the crystalline film texture of the columnar Al_2O_3/ZnO heterostructures grown by combining the SCS and ALD approaches. The 2θ angle of the XRD patterns ranges between 20° and 80° for ZnO, based on the PDF card #36-1451, for both the ZnO films and Al_2O_3/ZnO heterostructure samples with a film thickness of 15 nm after thermal annealing at 620 °C for 40 min, see **Figure 3**. Significant *hkil*

reflections correspond to the $(10\bar{1}0)$, (0002), $(10\bar{1}1)$, $(10\bar{1}2)$, $(11\bar{2}0)$, $(10\bar{1}3)$, $(11\bar{2}2)$ and $(20\bar{2}1)$ lattice planes of ZnO (pdf #36-1452, Zincite syn) at the 2θ values of 31.7°, 34.3°, 36.2°, 47.5°, 56.6°, 62.65°, 67.9° and 69.1°, respectively. No reflections associated with crystalline Al_2O_3 phases were detected in our experiments. By comparing the intensity distribution of the ZnO reflections in our samples with reference to XRD powder patterns of ZnO, we found that the increased intensity of the 0002 reflections indicates a certain crystalline texture in the film, suggesting that a high fraction of columnar ZnO grows along the *c*-axis direction parallel to the film surfaces. Assuming that longitudinal columnar growth always takes place along the *c*-axis in the wurtzite-type crystal structure, the powder-like intensity distribution further supports a large out-of-plane mistilt of the ZnO columns, which exposes the non-polar $(10\bar{1}0)$ surface to the environment, which is useful for gas detecting properties, as we will demonstrate later.

The room temperature micro-Raman spectrum of the Al_2O_3/ZnO heterostructures with an Al_2O_3 thickness of 15 nm after thermal annealing at 620 °C for 40 min is shown in **Figure 4**. The high-intensity peaks at 100 and 437 cm^{-1} can be assigned to the E_2(low) and E_2(high) modes of zinc oxide, accordingly [50,51]. Additional peaks at 210, 331, 384, 407, 570 and 580 cm^{-1} can be assigned to the $2E_2$(low) second-order mode E_2(low)-E_2(high), multiphonon scattering, A_1(TO), E_1(TO), A_1(LO) and E_1(LO) (superposition) modes of zinc oxide, respectively [51–53]. The Raman spectrum of the Al_2O_3/ZnO heterostructures after thermally annealing the columnar ZnO samples at 550 and 650 °C and coating them with a nano-layer of Al_2O_3 with a thickness of 7 nm followed by further thermal annealing at 620 °C for 40 min, is shown in **Figure S2**. No peaks associated with crystalline Al_2O_3 phases were detected, indicating that the exposed nanomaterial is an amorphous aluminum oxide layer.

The ZnO and Al_2O_3/ZnO thin films deposited over two different types of substrates, namely conventional microscope glass and quartz glass substrates, were also investigated by XPS. We observed a significant signal corresponding to sodium, in agreement with previous studies of samples grown on conventional glass slides using a similar deposition technique to the one used

here (see Supporting Information **Text S1** and **Figure S3**). The presence of Na is typically attributed to migration from the glass substrate to the sensor surface due to the elevated temperatures required to prepare the samples.[14] Given our choice of quartz glass as an alternative substrate, the presence of Na can be neglected to obtain a cleaner spectrum. In the investigated XPS spectrum (see **Figure 5**), the observed signals can be assigned to the elements Zn, O, C, and Al. It is important to point out that no signal of Zn was detected in the untreated Al_2O_3/ZnO thin films deposited on quartz glass, which is explained by a continuous and complete coating of the ZnO thin film by an overlayer of Al_2O_3, similar to the samples used for the TEM studies. Furthermore, in the spectra of both samples, namely ZnO and Al_2O_3/ZnO, the signal of C originates from environmental carbon compounds and was used to correct for potential charging. The high-resolution spectra of the O-1s, C-1s, Al-2p and Zn-2p lines are shown in **Figure 5**.

The Zn-2p$_{3/2}$ signal, with its peak position around 1022.0 eV, correlates well with Zn^{2+} in ZnO, which is usually reported between 1021.4 and 1022.5 eV. Furthermore, the peak separation of the Zn-2p$_{3/2}$ and Zn-2p$_{1/2}$ signals is 23.15 eV, which is within the expected range [32]. The XPS analysis indicates the presence of ZnO rather than metallic Zn, given the characteristic shape of the O-1s peak and the presence of the additional component around 530.0 eV [32,54].

The Al-2p line has its main peak at 73.7 eV, which corresponds well with Al^{3+} in Al_2O_3 which is frequently reported between 73.7 and 74.8 eV [32,54]. The obtained data are in good compliance with previous reports and confirm the high-quality nature of the nanomaterials used in our sensor studies.

3.2 Morphology of the Al_2O_3/ZnO heterostructures

Figure 6 shows the SEM images of the Al_2O_3/ZnO heterostructures coated using aluminum oxide with a thickness of 15 nm and subsequently thermally treated at 620 °C for 40 min in ambient air. For comparison purposes, **Figure S4** shows the Al_2O_3/ZnO heterostructures with an aluminum

oxide overlayer of 15 nm in thickness. Lower magnification SEM images (**Figure 6a**) show that nanocrystallites have grown to cover completely the glass substrate. **Figure 6b** shows films formed by interconnected columns that are merged over the entire surface, where they form favorable pathways for the flow of electricity through such samples. From **Figures 6c** and **6d**, we measured the average diameter (D) of the nanocrystallites, which is about 300 nm. The standard deviation of the grain diameter distribution was reported in our previous works [8,53]. Our current SEM measurements display the columnar shape of the nanostructures, see **Figure 6**, which compares well with the cross-section micrographs of the columnar films reported previously [8]. Due to the highly tilted columns, which form a very rough surface structure, the non-polar side facets are exposed to a large extent, acting as adsorption centers/sites for the VOC molecules during the sensor investigations. One of those active facets is the non-polar $(10\bar{1}0)$ surface, which has been extensively studied for gas sensing applications [55, 56], see **Figure S5**.

3.3. Gas sensing properties of the Al₂O₃/ZnO heterostructures

The sensing performances of the Al_2O_3/ZnO heterostructures with varying thicknesses of the Al_2O_3 layer ranging from 5-18 nm were investigated for several gases, including hydrogen, *n*-butanol, 2-propanol, ethanol, acetone and ammonia, at an operating/working temperature of 350 ℃, as reported in **Figure 7(a)**. The measured gas response values indicate that 12-15 nm of Al_2O_3 in the top layer leads to the highest response and largest selectivity towards 2-propanol vapor. The lowest response value to 2-propanol is 284%, which was measured for the sensor containing an Al_2O_3 coating layer with a thickness of just 5 nm, whereas the extraordinary response to 2-propanol, in the order of 2000%, is achieved for the sensor containing an aluminum oxide layer with a thickness of 15 nm. The gas response of the Al_2O_3/ZnO heterostructures with a thickness of 15 nm was measured several times over a period of two years. **Figure S6** shows that the response is essentially the same even after such a long period of time, which is very important for the use

of gas sensors in safety applications. For thicker coatings, the gas response values decrease drastically, since 15 nm is the maximum thickness of the top Al_2O_3 layer which still allows the ZnO underlayer of the heterojunction to participate in the sensing mechanism to 2-propanol. The influence of the thickness of the Al_2O_3 layer on the gas response value can be explained by the initial electrical resistance of the Al_2O_3/ZnO heterostructure. **Figure S7** shows the initial resistance of the Al_2O_3/ZnO heterostructure, which depends proportionally on the thickness of the Al_2O_3 top layer. **Figure S7** shows that as the thickness of the aluminum oxide layer increases, the initial electrical resistance of the heterostructure also increases. The lowest resistance value was obtained for the heterostructure with a top layer of only 5 nm thickness, and the highest resistance was obtained for the layer with a thickness of 18 nm. When exposed to 2-propanol vapor, different responses were observed depending on the thickness of the Al_2O_3 films deposited over the ZnO columns. The largest gas response was obtained for an optimum thickness of 15 nm. Sensors with a smaller or larger thickness of the Al_2O_3 layer have smaller responses. Sensors with thinner or thicker Al_2O_3 layers have lesser responses. From the experimental data, the gas reaction exhibits n-type semiconductor behavior, which means that the resistance to gas action decreases [17]. At a thickness of 5 nm, the electrical resistance of the aluminum oxide/zinc oxide heterojunction is the lowest, which means that the sensor only has a small number of electrons available to participate in the detection of 2-propanol vapors [17]. As the thickness of the aluminum oxide increases, so does the number of electrons involved in detecting 2-propanol vapor. Despite measuring the highest resistance for samples with a thickness of 18 nm for the Al_2O_3 layer deposited over ZnO columns, the gas response was lower, which is related to the tunneling lifetime of the charge carriers, which is longer for the samples with smaller thickness [17]. This can be justified based on the higher number of charge carriers and the shorter tunneling times, resulting in a thickness of 15 nm of the Al_2O_3 layer as optimal for the detection of 2-propanol vapors [17]. To provide more insight, we have performed computer simulations to rationalize the contribution of each component of the columnar

interface, i.e. the ZnO underlayer and the Al_2O_3 overlayer to the sensing mechanism, with the results reported in section 3.4.

To provide further insights into the properties of the sensor structure with a 15 nm thick layer of Al_2O_3 deposited over the columnar ZnO and to compare its performance to the untreated ZnO films, we also studied the response to the gases with a concentration of 100 ppm at diverse operating/working temperatures. **Figure 7(b)** displays the response to 2-propanol vapors, that takes place at operating/working temperatures equal to and above 200 °C, where the response value is the lowest at about 20%. Increasing the operating temperature leads to a rise in the gas response, which reaches the value of approximately 2000% at the operating temperature of 350 °C. In addition, the effect of the relative humidity on the 2-propanol response at an operating temperature of 350 °C was investigated for the ZnO films and Al_2O_3/ZnO heterostructures with a thickness of 15 nm for the Al_2O_3 nanolayer (see **Figure S8**). The gas response of the coated sensor drastically decreases by a factor of 10 at 40% of relative humidity. Compared to pure ZnO, it is evident that the Al_2O_3 overlayer protects the ZnO films against the effects of humidity, ensuring a high gas response. **Figure 7(b)** also shows the response to other gases, such as hydrogen and ethanol, which can be detected at an OPT temperature as low as 200 °C, whereas the response to acetone vapors appears only at an OPT temperature of 250 °C. **Figure 7(c)** provides evidence that the dynamic response curves of the sensor recover completely at the operating temperature of 350 °C after stopping the flow of each of the tested gases, i.e., hydrogen, ethanol, 2-propanol, *n*-butanol, and acetone, with a concentration each of 100 ppm. The gas response was determined as

$$S = \frac{\Delta G}{G_{air}} * 100\% = \frac{G_{gas} - G_{air}}{G_{air}} * 100\% \qquad (1)$$

where G_{air} is the conductance of the sample in air and G_{gas} is the conductance of the sample in the tested gases [57]. The response and recovery times for 2-propanol, which are shown in **Table S1**, have been defined in previous works [51,58] as the time required to achieve or recover 90% of the complete response. A comparison of parameters published in the literature for other sensors for 2-

propanol is shown in **Table S1**. The proposed gas sensing mechanism is described in the Supporting Information **Text S2**. Based on this investigation, the decreasing order of stability for the adsorption of the VOCs on the exposed sites is: *2-propanol > n-butanol ≈ ethanol > acetone*. **Figure S9** shows that the current-voltage characteristics show ohmic character/behavior at room temperature and operating temperatures of 150 and 200 °C. The *I-V* electrical curve changes at elevated operating/working temperatures between 250 and 350 °C, demonstrating the non-linear behavior of the sensor due to an increase of its conductivity [59–61]. It was also observed that the electrical current values are quite small, in the order of μA, up to the operating temperature of 200 °C. However, the value of the electrical current increases in the order of mA after raising the operating temperature from 250 to 350 °C, due to the increase in electrical conductivity [24,51,62].

3.4. Adsorption of molecules on the Al$_2$O$_3$/ZnO heterostructures. Ab-initio calculations of the sensor surface and interface.

To rationalize the experimental observations, we have performed comprehensive DFT calculations of our model of the sensor surface and interface, where we have considered the special surface morphology characterized by a large proportion of grains that expose non-polar side facets. An explanation for performing the calculations using the particular Al$_2$O$_3$/ZnO(10$\bar{1}$0) interface is presented in the Supporting Information **Text S3**. The XRD and SEM measurements suggest that the columnar zinc oxide film is *c*-textured and exhibits an "irregular"/rough surface structure, where the ZnO columns do not grow perpendicular to the surface normal and have conical shapes at the top [8]. This surface structure allows ZnO to expose a large fraction of side facets, which act as adsorption sites when exposed to the test gas. To provide further insight into the surface chemistry of the Al$_2$O$_3$/ZnO(10$\bar{1}$0) interface, we simulated the adsorption of a selection of VOCs comprising 2-propanol (2-C$_3$H$_7$OH), *n*-butanol (*n*-C$_4$H$_9$OH), ethanol (C$_2$H$_5$OH), and acetone (CH$_3$COCH$_3$), as well as hydrogen (H$_2$). Given the structure of the Al$_2$O$_3$/ZnO(10$\bar{1}$0) interface,

14

we explored the interaction of the VOCs *via* coordination of their O atom with the exposed Zn and Al species, while the adsorption of H_2 was calculated on the surface O atoms. For the binding configurations, the atoms forming the coordinate bond at the interface were initially placed at a distance of approximately, 1.5 Å and the entire systems were afterwards permitted to relax to their equilibrium adsorption geometries and energies, in line with our previous works [41–43,63]

The adsorption energies for the interactions of the molecules with the Al_2O_3/$ZnO(10\bar{1}0)$ interface are listed in **Table 1**. Our calculations suggest that the VOCs release the largest adsorption energies upon interaction with the surface Zn atoms, which are on average 0.3 to 0.8 eV more reactive than the Al dopant site. We found that the adsorption energies for the less favorable Al sites follow almost the same trends simulated for the Zn atoms. The H_2 molecule shows a preference by 0.316 eV for dissociative rather than molecular adsorption. Although still releasing slightly larger adsorption energy than the dissociative binding mode of H_2, the interaction of *n*-C_4H_9OH with the Al site displays the smallest adsorption energy of all VOCs at −0.450 eV. The calculated binding energies, at the most stable adsorption sites, reveal that the decreasing order of molecular preference for the Al_2O_3/$ZnO(10\bar{1}0)$ interface is 2-propanol (2-C_3H_7OH) ≈ *n*-butanol (*n*-C_4H_9OH) > ethanol (C_2H_5OH) > acetone (CH_3COCH_3) ≫ hydrogen (H_2). These binding strengths for the organic molecules on the Zn site agree with our gas response experiments. However, our molecular adsorption simulations are unable to capture the larger selectivity observed for H_2 with respect to acetone (CH_3COCH_3) in our gas sensing tests, which may be the result of other surfaces present in small proportions in the experimental morphology, that are not considered in our simulations. **Figure S10** shows the unit cell of the ZnO wurtzite-type structure.

We have also simulated the adsorption energies and charge transfers of the adsorbates on the pristine α-$Al_2O_3(0001)$ and $ZnO(10\bar{1}0)$ surfaces, which are listed in **Table 2**. We found that the adsorption energies on the Al_2O_3/$ZnO(10\bar{1}0)$ interface have intermediate values with respect to the parent materials. This explains that the vapour molecules do not bind too strongly, poisoning the interface and preventing the interaction and detection of other molecules. On the other hand,

the largest charge transfers were obtained for the interaction with the $Al_2O_3/ZnO(10\bar{1}0)$ interface, supporting the strong signal measured during the gas sensing experiments.

Figure 8 illustrates the most stable binding modes for the adsorption of the molecules investigated here, *i.e.* the VOCs and H_2, on the surface of the $Al_2O_3/ZnO(10\bar{1}0)$ interface. As discussed previously, the alcohols and the ketone show the largest preference for the Zn site, where the Zn−O coordinate bond distances formed range from 2.08 to 2.12 Å. We also found evidence that the alcohols form a hydrogen bond with a nearby surface O atom in a secondary interaction. The longest hydrogen-bond distance of 2.30 Å was calculated for the most stable adsorption mode of 2-propanol ($2\text{-}C_3H_7OH$), while the shortest hydrogen-bond of 1.99 Å was predicted for ethanol (C_2H_5OH). Our simulations suggest that there is an inverse correlation between the adsorption energy of the alcohols and the distance of the hydrogen-bond formed with the surface. By comparing the average adsorption energies of the alcohols with the value for the ketone, we estimate that the formation of the hydrogen-bonds accounts for around 0.3 eV. The alkyl radical of the alcohols containing up to three C atoms lies almost parallel to the surface, but it accommodates itself perpendicularly to the surface for *n*-butanol ($n\text{-}C_4H_9OH$). The H_2 molecule dissociates upon adsorption, with the H atoms forming OH groups with the surface O ions. The mean O−H bond distance is 0.99 Å, which is typical of hydroxyl groups, while the separation between the dissociated H atoms was computed at 6.82 Å.

We next fulfill/performed a Bader charge analysis to rationalise the trends obtained for the adsorption energies. **Table 1** lists the charges transferred upon the interaction between the adsorbates and the surface. For the least favorable adsorption modes on the Al sites, we found that the VOCs gain electron density from the surface and become negatively charged. The charge density donated by the surface in the least stable binding configurations was calculated between -0.019 and -0.021 e$^-$ for the VOCs, apart from ethanol (C_2H_5OH) which gained a more modest value of -0.013 e$^-$. We also found evidence of charge density migration of -0.011 e$^-$ from the surface to the adsorbed H_2 molecule. In contrast, the VOCs and H_2 lost electron density to the

16

surface in the interactions with the most sensitive Zn site and when H_2 is adsorbed dissociatively, respectively. Our calculations reveal that in the adsorption of the alcohols at the Zn atoms, they donated more than twice the charge gained from the surface in the interactions with the Al sites. In particular, the H_2 molecule transferred 1.181 e⁻ during its dissociative adsorption, which is the largest charge flow observed in this work. Our DFT-calculated charges show that the electron densities donated by the VOCs at the Zn sites follow the same trend as the adsorption energies, validating the coordinate nature of the bond formed at the molecule/surface interface. **Figure 9** displays the charge density difference ($\Delta\rho$) for the most exothermic binding configurations and for the atoms that experienced the largest electron density change. Note that the charge density differences were calculated as $\Delta\rho = \rho_{ads} - \rho_{mol} - \rho_{sur}$, where ρ_{ads}, ρ_{mol} and ρ_{sur} represent the charge density of the adsorption, the isolated molecule, and the isolated surface, respectively, with identical structure. **Figure 9a-c** illustrates that the alcohols lost between 0.043 and 0.054 e⁻ of charge during adsorption, whereas the hydroxyl O received −0.036 to −0.074 e⁻ from the coordinated Zn atom, which donated 0.052 to 0.058 e⁻. Moreover, the hydroxyl H, which is involved in the hydrogen-bond between the alcohols and the surface, saw its electron charge reduced by 0.047 to 0.095 e⁻, which was incorporated by a nearby surface O atom, that increased its charge by −0.036 to −0.045 e⁻. The O atom from the acetone (CH_3COCH_3) molecule accepted −0.053 e⁻ to reach a total charge of −1.127 e⁻, whereas the coordinated Zn atom depleted its electron density by 0.065 e⁻, see **Figure 9d**. The atoms from the alkyl chain of the VOCs containing fewer than four C atoms, which adsorb parallel to the surface, also experienced significant charge transfers, indicating the existence of weak Coulomb attraction forces between the adsorbate and the sensor. **Figure 9e** shows that each of the H atoms donated over 0.5 e⁻ of charge, in one case to the O atom forming the structural OH group and in the other case to a nearby surface anion that establishes a hydrogen bond, which gained between −0.261 and −0.493 e⁻ of electron density.

To provide further insight into the electronic properties of the most exothermic adsorption configurations, we have calculated the projection of the density of states (PDOS) onto the interacting atoms, as shown in **Figure 10**. The PDOS of the p states of the Zn atoms are negligible and are therefore not discussed. **Figure 10a-d** shows that the Zn valence d states appear between the Fermi level and -7.0 eV, with the centre of the largest PDOS calculated at around -5.5 eV. The Zn d states do not display any virtual band below 2.5 eV, indicating that the surfaces are large bandgap insulators. Despite the minor differences observed on the d states of Zn, the O p orbitals of the adsorbates show discrete peaks with their positions slightly shifted for the different molecular adsorptions. For example, the alcohols have three bands at approximately -9.75, -7.5 and -6.25 eV as well as a shoulder within the range of -2.0 to -5.5 eV. However, the ketone displays mostly isolated bands that are away from the Fermi level with respect to the alcohols. Our PDOS for the interaction of the VOCs with the sensor shows minimal hybridisation between the d and p states of the Zn and O atoms, respectively, confirming that these atoms form a coordinate bond with moderate charge transfers. For the dissociative adsorption of H_2, the surface O atoms forming the structural hydroxyl groups have a broad band between -1.25 and -9.75 eV and two distinctive bands at -9.5 and -7.7 eV, see **Figure 10e**. The dissociated H atoms have an s band each, which are strongly hybridised with the isolated bands of the surface O atoms, providing further evidence for the covalent bond formed between these atoms and explaining the large charge transfer calculated for this adsorption configuration.

To summarise our DFT calculations of the adsorption of VOCs, which are in excellent unison/agreement with the gas response investigations, we predict that 2-C_3H_7OH releases the largest adsorption energy when it interacts with the $Al_2O_3/ZnO(10\bar{1}0)$ surface. The interaction between our model of the nanostructured sensor and the secondary alcohol is characterized by one interfacial Zn$-$O coordination bond and a secondary interaction in the form of a hydrogen-bond between the adsorbate and the surface. The alkyl radical of 2-C_3H_7OH lies parallel to the surface due to weak Coulomb attractive forces. The O atom of 2-C_3H_7OH donates electronic charge to the

coordinated Zn cation, as confirmed by the Bader analysis and projection of the density of states, which is typical of coordinative covalent bonds.

4. Conclusions

The Al_2O_3/ZnO heterostructure-based sensors deposited on different substrates were successfully obtained using an SCS approach in combination with a new high-aspect-ratio ALD method, in which coatings of Al_2O_3 ultra-thin films with a thickness of between 3 and 18 nm were deposited on top of columnar ZnO films. The reliability of this process was demonstrated by TEM studies on suitable model systems. The morphological, microtopological, nanostructural, electrical, and gas sensing performances of these sensors were fully characterized. The analysis of the morphology of the sensors revealed that as grown, interconnected, and interpenetrated nanocrystallites of the columnar ZnO underlayer were covered by a thin overlayer of Al_2O_3. The structural studies confirmed the formation of the Al_2O_3/ZnO heterostructures, whereas the TEM measurements validated the thickness of the Al_2O_3 layers between 3 and 18 nm. The morphological and structural characterization of the ZnO film revealed a rough surface composed of protruding and interpenetrating columnar grains grown with a distinct 0002-texture and a large out-of-plane tilt, suggesting a dominant fraction of exposed $(10\bar{1}0)$ side facets in the total surface area of the sensor.

We found that the best response is obtained at a nominal thickness of the aluminum oxide overlayer of 15 nm deposited on top of the columnar ZnO underlayer. By gradually increasing the thicknesses of Al_2O_3 to 15 nm, we improved the response to 2-propanol to the highest selectivity of ~2000% at the OPT of 350 °C.

We also calculated the adsorption modes, structures, and electronic properties of the interaction of a series of VOC molecules and H_2 with the Al_2O_3/ZnO$(10\bar{1}0)$ interface using DFT −D2 methods, to identify the contribution of this junction to the sensing mechanism. We first

obtained the relevant $Al_2O_3/ZnO(10\bar{1}0)$ interface structure by replacing three Zn atoms with two Al atoms, and identified the most stable structure where two subsurface Zn atoms had been replaced by Al atoms, while removing a nearby subsurface Zn atom to keep the system electrically neutral. We calculated negative adsorption energies for the interaction of all the molecules studied here with the interface, indicating that these are spontaneous processes. The Zn sites are more reactive than the Al dopant atoms, indicated by the relative exothermicity of the molecular adsorptions at the two sites. The adsorbates acquired electron charge upon binding to the Al sites, but donated electron densities in their interactions with the Zn site, supporting the coordinative nature of the bond formed between the adsorbate and the sensor. The decreasing order of stability for the adsorption of the VOCs on the Zn site is $E_{ads}(2\text{-}C_3H_7OH) \approx E_{ads}(n\text{-}C_4H_9OH) > E_{ads}(C_2H_5OH) > E_{ads}(CH_3COCH_3)$. The alkyl radical chain of the VOCs with up to three C atoms becomes flat after adsorption to facilitate small charge transfers with the surface. Based on the local density of states analysis, we have determined the fundamental role of the Zn d states and molecular O p orbitals in the interaction between the adsorbates and the sensor. The strong hybridization of the H s electron and the interacting surface O p states evidence the covalent character of the bond formed during the dissociative adsorption of H_2.

To conclude, this study confirmed the successful synthesis of Al_2O_3/ZnO heterostructures and their suitability as a new sensor device for the detection of VOCs. We have demonstrated that a thorough optimization of technological approaches, especially by combining different methods like SCS and ALD, and enhancement of surface properties, by creating heterostructured nano-materials, improves the gas response to 2-propanol and n-butanol in real applications. The results obtained are highly important for practical applications, as well as for further fundamental studies of the junction effects on the sensing mechanism of VOC sensors based on semiconducting metal oxides.

■ **ASSOCIATED CONTENT**

Supporting Information: Structure of the 2x2 supercell of the ZnO (10$\bar{1}$0) surface simulated using DFT calculations. Micro-Raman spectra of the ZnO films and Al_2O_3/ZnO heterostructures with thermal annealing of ZnO at 550 ^{o}C and 650 ^{o}C and with nano-layer of Al_2O_3 with a thickness of 7 nm treated with thermal annealing/treatment at 620 ^{o}C for 40 min. XPS spectra and related discussion of the Al_2O_3/ZnO heterostructures deposited over glass substrates. SEM results of the Al_2O_3/ZnO heterostructures with a thickness of 15 nm of Al_2O_3. Crystallographic structure of ZnO showing the shape of a hexagonal prism and the planes (0001), (000$\bar{1}$) and (10$\bar{1}$0). Variation of the gas response to 2-propanol vapors over time for the Al_2O_3/ZnO heterostructures with a thickness of 15 nm for the Al_2O_3 overlayer. The initial electrical resistance of the Al_2O_3/ZnO heterostructure depends on the thickness of the Al_2O_3 film. The influence of relative humidity in the response to 2-propanol at different relative humidity values of the ZnO films and Al_2O_3/ZnO heterostructures. Comparison of the reported 2-propanol sensors with high gas response values. Scheme of the suggested gas detection/sensing mechanism. Current-Voltage characteristics and related discussion of a ZnO/Al_2O_3 heterostructure sensor with 15 nm Al_2O_3 layer thickness at different operating temperatures. The unit cell of the ZnO wurtzite-type structure. The Supporting Information is available free of charge on the ACS Publications website at http://pubs.acs.org

■ AUTHOR INFORMATION

Corresponding Authors
*E-mails: ollu@tf.uni-kiel.de, oleg.lupan@mib.utm.md (O.L.); d.santos-carballal@leeds.ac.uk (D.S.C.); lk@tf.uni-kiel.de (L.K.); ra@tf.uni-kiel.de (R.A.); alva@tf.uni-kiel.de (A.V.); sn@tf.uni-kiel.de (S.N.).

Notes
The authors declare no competing interest.

AUTHOR CONTRIBUTIONS

O.L., N.M., M.T.B., and S.H. have prepared the materials and developed the deposition approach. A.V. carried out all XPS experiments, analyzed the XPS data and drafted part for the article. O.L., N.M., R.A. and S.N. fitted a technological strategy and experiments for material incorporation into the devices for detecting VOCs. N.M., N.A., H.K. and O.L. carried out the characterization of the materials, analyzed the data, and wrote part of the draft of the article. M.T.B carried out laboratory research of the alumina ALD. O.L., N.M, D.S.-C., A.K.M., N.A., A.V., N.H.d.L., R.A., H.K. and S.H. analyzed the data from experiments and contributed writing the manuscript. D.S.-C., A.K.M. and N.H.d.L. carried out the DFT simulations and drafted the computational part for the manuscript. O.L., N.M., S.N., R.A., L.K., N.H.d.L. and D.S.-C. conceived and designed the study and gave the final approval of the draft to be submitted and published. N.K., N.W., and L.K carried out TEM laboratory research, investigations, analyzed the TEM results and drafted part for the article. O.L., S.H., L.K. and R.A. performed the design and conception of the studies. The work was written based on contributions by all authors, who all reviewed the manuscript.

■ **References**

(1)   Lin, T.; Lv, X.; Hu, Z.; Xu, A.; Feng, C. Semiconductor Metal Oxides as Chemoresistive Sensors for Detecting Volatile Organic Compounds. *Sensors (Switzerland)* **2019**, *19* (2), 233. https://doi.org/10.3390/s19020233.

(2)   Zappa, D.; Galstyan, V.; Kaur, N.; Munasinghe Arachchige, H. M. M.; Sisman, O.; Comini, E. "Metal Oxide -Based Heterostructures for Gas Sensors"- A Review. *Anal. Chim. Acta* **2018**, *1039*, 1–23.

https://doi.org/10.1016/j.aca.2018.09.020.

(3)   Li, T.; Zeng, W.; Wang, Z. Quasi-One-Dimensional Metal-Oxide-Based Heterostructural Gas-Sensing Materials: A Review. *Sensors Actuators, B Chem.* **2015**, *221*, 1570–1585. https://doi.org/10.1016/j.snb.2015.08.003.

(4)   Choi, S. J.; Kim, I. D. Recent Developments in 2D Nanomaterials for Chemiresistive-Type Gas Sensors. *Electron. Mater. Lett.* **2018**, *14* (3), 221–260. https://doi.org/10.1007/s13391-018-0044-z.

(5)   Lupan, O.; Ababii, N.; Mishra, A. K.; Bodduluri, M. T.; Magariu, N.; Vahl, A.; Krüger, H.; Wagner, B.; Faupel, F.; Adelung, R.; de Leeuw, N. H.; Hansen, S. Heterostructure-Based Devices with Enhanced Humidity Stability for H_2 Gas Sensing Applications in Breath Tests and Portable Batteries. *Sensors Actuators, A Phys.* **2021**, *329*, 112804. https://doi.org/10.1016/j.sna.2021.112804.

(6)   Galstyan, V.; Kaur, N.; Zappa, D.; Núñez-Carmona, E.; Sberveglieri, V.; Comini, E. Chemical Gas Sensors Studied at SENSOR Lab, Brescia (Italy): From Conventional to Energy-Efficient and Biocompatible Composite Structures. *Sensors (Switzerland)* **2020**, *20* (3), 579. https://doi.org/10.3390/s20030579.

(7)   Cretu, V.; Postica, V.; Mishra, A. K.; Hoppe, M.; Tiginyanu, I.; Mishra, Y. K.; Chow, L.; De Leeuw, N. H.; Adelung, R.; Lupan, O. Synthesis, Characterization and DFT Studies of Zinc-Doped Copper Oxide Nanocrystals for Gas Sensing Applications. *J. Mater. Chem. A* **2016**, *4* (17), 6527–6539. https://doi.org/10.1039/c6ta01355d.

(8)   Lupan, C.; Khaledialidusti, R.; Mishra, A. K.; Postica, V.; Terasa, M. I.; Magariu, N.; Pauporté, T.; Viana, B.; Drewes, J.; Vahl, A.; Faupel, F.; Adelung, R. Pd-Functionalized ZnO:Eu Columnar Films for Room-Temperature Hydrogen Gas Sensing: A Combined Experimental and Computational Approach. *ACS Appl. Mater. Interfaces* **2020**, *12* (22), 24951–24964. https://doi.org/10.1021/acsami.0c02103.

(9)   Hübner, M.; Simion, C. E.; Tomescu-Stǎnoiu, A.; Pokhrel, S.; Bârsan, N.; Weimar, U. Influence of Humidity on CO Sensing with P-Type CuO Thick Film Gas Sensors. *Sensors Actuators, B Chem.* **2011**, *153* (2), 347–353. https://doi.org/10.1016/j.snb.2010.10.046.

(10)   Kohlmann, N.; Hansen, L.; Lupan, C.; Schürmann, U.; Reimers, A.; Schütt, F.; Adelung, R.; Kersten, H.; Kienle, L. Fabrication of ZnO Nanobrushes by H_2–C_2H_2 Plasma Etching for H_2 Sensing Applications. *ACS Appl. Mater. Interfaces* **2021**, *13* (51), 61758–61769. https://doi.org/10.1021/acsami.1c18679.

(11)   Kwon, J. H.; Jeong, E. G.; Jeon, Y.; Kim, D.-G.; Lee, S.; Choi, K. C. Design of Highly Water Resistant, Impermeable, and Flexible Thin-Film Encapsulation Based on Inorganic/Organic Hybrid Layers. *ACS Appl. Mater. Interfaces* **2019**, *11* (3), 3251–3261. https://doi.org/10.1021/acsami.8b11930.

(12)   LIU, X.-P.; PENG, B.; ZHANG, W.-L.; ZHU, J. Al_2O_3 Coating Layer on the High Temperature Conductive Stability of Pt/ZnO/Al_2O_3 Film Electrode. *J. Inorg. Mater.* **2019**, *34* (6), 605. https://doi.org/10.15541/jim20180352.

(13)   French, P.; Krijnen, G.; Roozeboom, F. Precision in Harsh Environments. *Microsystems Nanoeng.* **2016**, *2* (1), 16048. https://doi.org/10.1038/micronano.2016.48.

(14)   Ababii, N.; Hoppe, M.; Shree, S.; Vahl, A.; Ulfa, M.; Pauporté, T.; Viana, B.; Cretu, V.; Magariu, N.; Postica, V.; Sontea, V.; Terasa, M. I.; Polonskyi, O.; Faupel, F.; Adelung, R.; Lupan, O. Effect of Noble Metal Functionalization and Film Thickness on Sensing Properties of Sprayed TiO_2 Ultra-Thin Films. *Sensors Actuators, A Phys.* **2019**, *293*, 242–258. https://doi.org/10.1016/j.sna.2019.04.017.

(15)   Das, A.; Patra, M.; Hazarika, M.; Nair, R. G. ZnO-In_2O_3 Nanocomposite: An Efficient Solar Photocatalyst. In *AIP Conference Proceedings*; 2019; Vol. 2100, p 020033. https://doi.org/10.1063/1.5098587.

(16)   Bigiani, L.; Zappa, D.; Maccato, C.; Gasparotto, A.; Sada, C.; Comini, E.; Barreca, D. Mn_3O_4 Nanomaterials Functionalized with Fe_2O_3 and ZnO: Fabrication, Characterization, and Ammonia Sensing Properties. *Adv. Mater. Interfaces* **2019**, *6* (24), 1901239. https://doi.org/10.1002/admi.201901239.

(17)   Kim, J.-H.; Mirzaei, A.; Kim, H. W.; Kim, S. S. Variation of Shell Thickness in ZnO-SnO_2 Core-Shell

Nanowires for Optimizing Sensing Behaviors to CO, C_6H_6, and C_7H_8 Gases. *Sensors Actuators B Chem.* **2020**, *302*, 127150. https://doi.org/10.1016/j.snb.2019.127150.

(18) Kim, J.-H.; Lee, J.-H.; Park, Y.; Kim, J.-Y.; Mirzaei, A.; Kim, H. W.; Kim, S. S. Toluene- and Benzene-Selective Gas Sensors Based on Pt- and Pd-Functionalized ZnO Nanowires in Self-Heating Mode. *Sensors Actuators B Chem.* **2019**, *294*, 78–88. https://doi.org/10.1016/j.snb.2019.05.032.

(19) Kim, J.-H.; Wu, P.; Kim, H. W.; Kim, S. S. Highly Selective Sensing of CO, C_6H_6 , and C_7H_8 Gases by Catalytic Functionalization with Metal Nanoparticles. *ACS Appl. Mater. Interfaces* **2016**, *8* (11), 7173–7183. https://doi.org/10.1021/acsami.6b01116.

(20) Liu, Z.; Yang, P. Optoelectronic Performances on Different Structures of Al-Doped ZnO. *J. Am. Ceram. Soc.* **2018**, *101* (12), 5615–5626. https://doi.org/10.1111/jace.15818.

(21) Li, C.; Han, C.; Zhang, Y.; Zang, Z.; Wang, M.; Tang, X.; Du, J. Enhanced Photoresponse of Self-Powered Perovskite Photodetector Based on ZnO Nanoparticles Decorated $CsPbBr_3$ Films. *Sol. Energy Mater. Sol. Cells* **2017**, *172*, 341–346. https://doi.org/10.1016/j.solmat.2017.08.014.

(22) Kuo, T. J.; Lin, C. N.; Kuo, C. L.; Huang, M. H. Growth of Ultralong ZnO Nanowires on Silicon Substrates by Vapor Transport and Their Use as Recyclable Photocatalysts. *Chem. Mater.* **2007**, *19* (21), 5143–5147. https://doi.org/10.1021/cm071568a.

(23) Saito, N.; Haneda, H.; Sekiguchi, T.; Ohashi, N.; Sakaguchi, I.; Koumoto, K. Low-Temperature Fabrication of Light-Emitting Zinc Oxide Micropatterns Using Self-Assembled Monolayers. *Adv. Mater.* **2002**, *14* (6), 418–421. https://doi.org/10.1002/1521-4095(20020318)14:6<418::AID-ADMA418>3.0.CO;2-K.

(24) Lupan, O.; Chow, L.; Shishiyanu, S.; Monaico, E.; Shishiyanu, T.; Şontea, V.; Roldan Cuenya, B.; Naitabdi, A.; Park, S.; Schulte, A. Nanostructured Zinc Oxide Films Synthesized by Successive Chemical Solution Deposition for Gas Sensor Applications. *Mater. Res. Bull.* **2009**, *44* (1), 63–69. https://doi.org/10.1016/j.materresbull.2008.04.006.

(25) Lupan, O.; Shishiyanu, S.; Chow, L.; Shishiyanu, T. Nanostructured Zinc Oxide Gas Sensors by Successive Ionic Layer Adsorption and Reaction Method and Rapid Photothermal Processing. *Thin Solid Films* **2008**, *516* (10), 3338–3345. https://doi.org/10.1016/j.tsf.2007.10.104.

(26) Shishiyanu, S. T.; Lupan, O. I.; Monaico, E. V.; Ursaki, V. V.; Shishiyanu, T. S.; Tiginyanu, I. M. Photoluminescence of Chemical Bath Deposited ZnO:Al Films Treated by Rapid Thermal Annealing. *Thin Solid Films* **2005**, *488* (1–2), 15–19. https://doi.org/10.1016/j.tsf.2005.04.004.

(27) Lupan, O. I.; Shishiyanu, S. T.; Shishiyanu, T. S. Nitrogen Oxides and Ammonia Sensing Characteristics of SILAR Deposited ZnO Thin Film. *Superlattices Microstruct.* **2007**, *42* (1–6), 375–378. https://doi.org/10.1016/j.spmi.2007.04.009.

(28) Shishiyanu, S. T.; Shishiyanu, T. S.; Lupan, O. I. Sensing Characteristics of Tin-Doped ZnO Thin Films as NO_2 Gas Sensor. *Sensors Actuators, B Chem.* **2005**, *107* (1 SPEC. ISS.), 379–386. https://doi.org/10.1016/j.snb.2004.10.030.

(29) Shishiyanu, S. T.; Shishiyanu, T. S.; Lupan, O. I. Novel NO_2 Gas Sensor Based on Cuprous Oxide Thin Films. *Sensors Actuators, B Chem.* **2006**, *113* (1), 468–476. https://doi.org/10.1016/j.snb.2005.03.061.

(30) Paulowicz, I.; Postica, V.; Lupan, O.; Wolff, N.; Shree, S.; Cojocaru, A.; Deng, M.; Mishra, Y. K.; Tiginyanu, I.; Kienle, L.; Adelung, R. Zinc Oxide Nanotetrapods with Four Different Arm Morphologies for Versatile Nanosensors. *Sensors Actuators B Chem.* **2018**, *262*, 425–435. https://doi.org/10.1016/j.snb.2018.01.206.

(31) Gapeeva, A.; Boddururi, M. T.; Kaps, S.; Rasch, F.; Wagner, B.; Adelung, R.; Lupan, O. Mechanical and Wetting Properties of Three-Dimensional Flexible Tetrapodal ZnO Networks ALD-Coated with Al_2O_3. In *IFMBE Proceedings*; Tiginyanu, I., Sontea, V., Railean, S., Eds.; Springer International Publishing: Cham, 2020; Vol. 77, pp 263–267. https://doi.org/10.1007/978-3-030-31866-6_52.

(32) Moulder, J. F.; Stickle, W. F.; Sobol, P. E.; Bomben, K. D. Handbook of X-Ray Photoelectron Spectroscopy; Perkin-Elmer Corporation: Eden Prairie, MN, 1992. *Google Sch. There is no Corresp. Rec. this Ref.* **1992**, 52–53.

(33) Lupan, O.; Magariu, N.; Khaledialidusti, R.; Mishra, A. K.; Hansen, S.; Krüger, H.; Postica, V.; Heinrich, H.; Viana, B.; Ono, L. K.; Cuenya, B. R.; Chow, L.; Adelung, R.; Pauporté, T. Comparison of Thermal Annealing versus Hydrothermal Treatment Effects on the Detection Performances of

ZnO Nanowires. *ACS Appl. Mater. Interfaces* **2021**, *13* (8), 10537–10552. https://doi.org/10.1021/acsami.0c19170.

(34) Perdew, J. P.; Burke, K.; Ernzerhof, M. Generalized Gradient Approximation Made Simple. *Phys. Rev. Lett.* **1996**, *77* (18), 3865–3868. https://doi.org/10.1103/PhysRevLett.77.3865.

(35) Blöchl, P. E. Projector Augmented-Wave Method. *Phys. Rev. B* **1994**, *50* (24), 17953–17979. https://doi.org/10.1103/PhysRevB.50.17953.

(36) Joubert, D. From Ultrasoft Pseudopotentials to the Projector Augmented-Wave Method. *Phys. Rev. B - Condens. Matter Mater. Phys.* **1999**, *59* (3), 1758–1775. https://doi.org/10.1103/PhysRevB.59.1758.

(37) Kresse, G.; Hafner, J. Ab Initio Molecular Dynamics for Liquid Metals. *Phys. Rev. B* **1993**, *47* (1), 558–561. https://doi.org/10.1103/PhysRevB.47.558.

(38) Kresse, G.; Hafner, J. Ab Initio Molecular-Dynamics Simulation of the Liquid-Metalamorphous-Semiconductor Transition in Germanium. *Phys. Rev. B* **1994**, *49* (20), 14251–14269. https://doi.org/10.1103/PhysRevB.49.14251.

(39) Kresse, G.; Furthmüller, J. Efficiency of Ab-Initio Total Energy Calculations for Metals and Semiconductors Using a Plane-Wave Basis Set. *Comput. Mater. Sci.* **1996**, *6* (1), 15–50. https://doi.org/10.1016/0927-0256(96)00008-0.

(40) Kresse, G.; Furthmüller, J. Efficient Iterative Schemes for Ab Initio Total-Energy Calculations Using a Plane-Wave Basis Set. *Phys. Rev. B - Condens. Matter Mater. Phys.* **1996**, *54* (16), 11169–11186. https://doi.org/10.1103/PhysRevB.54.11169.

(41) Postica, V.; Vahl, A.; Strobel, J.; Santos-Carballal, D.; Lupan, O.; Cadi-Essadek, A.; De Leeuw, N. H.; Schütt, F.; Polonskyi, O.; Strunskus, T.; Baum, M.; Kienle, L.; Adelung, R.; Faupel, F. Tuning Doping and Surface Functionalization of Columnar Oxide Films for Volatile Organic Compound Sensing: Experiments and Theory. *J. Mater. Chem. A* **2018**, *6* (46), 23669–23682. https://doi.org/10.1039/C8TA08985J.

(42) Vahl, A.; Lupan, O.; Santos-Carballal, D.; Postica, V.; Hansen, S.; Cavers, H.; Wolff, N.; Terasa, M. I.; Hoppe, M.; Cadi-Essadek, A.; Dankwort, T.; Kienle, L.; De Leeuw, N. H.; Adelung, R.; Faupel, F. Surface Functionalization of ZnO:Ag Columnar Thin Films with AgAu and AgPt Bimetallic Alloy Nanoparticles as an Efficient Pathway for Highly Sensitive Gas Discrimination and Early Hazard Detection in Batteries. *J. Mater. Chem. A* **2020**, *8* (32), 16246–16264. https://doi.org/10.1039/d0ta03224g.

(43) Postica, V.; Vahl, A.; Santos-Carballal, D.; Dankwort, T.; Kienle, L.; Hoppe, M.; Cadi-Essadek, A.; De Leeuw, N. H.; Terasa, M. I.; Adelung, R.; Faupel, F.; Lupan, O. Tuning ZnO Sensors Reactivity toward Volatile Organic Compounds via Ag Doping and Nanoparticle Functionalization. *ACS Appl. Mater. Interfaces* **2019**, *11* (34), 31452–31466. https://doi.org/10.1021/acsami.9b07275.

(44) Monkhorst, H. J.; Pack, J. D. Special Points for Brillouin-Zone Integrations. *Phys. Rev. B* **1976**, *13* (12), 5188–5192. https://doi.org/10.1103/PhysRevB.13.5188.

(45) Cooke, D. J.; Marmier, A.; Parker, S. C. Surface Structure of (10$\bar{1}$0) and (1120) Surfaces of ZnO with Density Functional Theory and Atomistic Simulation. *J. Phys. Chem. B* **2006**, *110* (15), 7985–7991. https://doi.org/10.1021/jp0564445.

(46) Wander, A.; Harrison, N. M. Ab-Initio Study of ZnO(1120). *Surf. Sci.* **2000**, *468* (1–3), L851–L855. https://doi.org/10.1016/S0039-6028(00)00794-9.

(47) Grimme, S. Semiempirical GGA-Type Density Functional Constructed with a Long-Range Dispersion Correction. *J. Comput. Chem.* **2006**, *27* (15), 1787–1799. https://doi.org/10.1002/jcc.20495.

(48) Henkelman, G.; Arnaldsson, A.; Jónsson, H. A Fast and Robust Algorithm for Bader Decomposition of Charge Density. *Comput. Mater. Sci.* **2006**, *36* (3), 354–360. https://doi.org/10.1016/j.commatsci.2005.04.010.

(49) Orville-Thomas, W. J. Atoms in Molecules — a Quantum Theory. *J. Mol. Struct. THEOCHEM* **1996**, *360* (1–3), 175. https://doi.org/10.1016/S0166-1280(96)90925-2.

(50) Decremps, F.; Pellicer-Porres, J.; Saitta, A. M.; Chervin, J.-C.; Polian, A. High-Pressure Raman Spectroscopy Study of Wurtzite ZnO. *Phys. Rev. B* **2002**, *65* (9), 092101. https://doi.org/10.1103/PhysRevB.65.092101.

(51) Hoppe, M.; Lupan, O.; Postica, V.; Wolff, N.; Duppel, V.; Kienle, L.; Tiginyanu, I.; Adelung, R. $ZnAl_2O_4$-Functionalized Zinc Oxide Microstructures for Highly Selective Hydrogen Gas Sensing Applications. *Phys. status solidi* **2018**, *215* (7), 1700772. https://doi.org/10.1002/pssa.201700772.

(52) Cuscó, R.; Alarcón-Lladó, E.; Ibáñez, J.; Artús, L.; Jiménez, J.; Wang, B.; Callahan, M. J. Temperature Dependence of Raman Scattering in ZnO. *Phys. Rev. B - Condens. Matter Mater. Phys.* **2007**, *75* (16), 165202. https://doi.org/10.1103/PhysRevB.75.165202.

(53) Postica, V.; Hölken, I.; Schneider, V.; Kaidas, V.; Polonskyi, O.; Cretu, V.; Tiginyanu, I.; Faupel, F.; Adelung, R.; Lupan, O. Multifunctional Device Based on ZnO:Fe Nanostructured Films with Enhanced UV and Ultra-Fast Ethanol Vapour Sensing. *Mater. Sci. Semicond. Process.* **2016**, *49*, 20–33. https://doi.org/10.1016/j.mssp.2016.03.024.

(54) Naumkin, A. V; Kraust-Vass, A.; Gaarenstroom, S. W.; Powell, C. J. NIST X-ray Photoelectron Spectroscopy Database, National Institute of Standards and Technology. https://doi.org/10.18434/T4T88K.

(55) Patolsky, F.; Timko, B. P.; Zheng, G.; Lieber, C. M. Nanowire-Based Nanoelectronic Devices in the Life Sciences. *MRS Bull.* **2007**, *32* (2), 142–149. https://doi.org/10.1557/mrs2007.47.

(56) Pan, Z. W.; Dai, Z. R.; Wang, Z. L. Nanobelts of Semiconducting Oxides. *Science (80-.).* **2001**, *291* (5510), 1947–1949. https://doi.org/10.1126/science.1058120.

(57) Kutukov, P.; Rumyantseva, M.; Krivetskiy, V.; Filatova, D.; Batuk, M.; Hadermann, J.; Khmelevsky, N.; Aksenenko, A.; Gaskov, A. Influence of Mono- and Bimetallic PtO_x, PdO_x, $PtPdO_x$ Clusters on CO Sensing by SnO_2 Based Gas Sensors. *Nanomaterials* **2018**, *8* (11), 917. https://doi.org/10.3390/nano8110917.

(58) Lupan, O.; Postica, V.; Gröttrup, J.; Mishra, A. K.; de Leeuw, N. H.; Adelung, R. Enhanced UV and Ethanol Vapour Sensing of a Single 3-D ZnO Tetrapod Alloyed with Fe_2O_3 Nanoparticles. *Sensors Actuators B Chem.* **2017**, *245*, 448–461. https://doi.org/10.1016/j.snb.2017.01.107.

(59) Vahl, A.; Dittmann, J.; Jetter, J.; Veziroglu, S.; Shree, S.; Ababii, N.; Lupan, O.; Aktas, O. C.; Strunskus, T.; Quandt, E.; Adelung, R.; Sharma, S. K.; Faupel, F. The Impact of O_2/Ar Ratio on Morphology and Functional Properties in Reactive Sputtering of Metal Oxide Thin Films. *Nanotechnology* **2019**, *30* (23), 235603. https://doi.org/10.1088/1361-6528/ab0837.

(60) Lupan, O.; Cretu, V.; Postica, V.; Ababii, N.; Polonskyi, O.; Kaidas, V.; Schütt, F.; Mishra, Y. K.; Monaico, E.; Tiginyanu, I.; Sontea, V.; Strunskus, T.; Faupel, F.; Adelung, R. Enhanced Ethanol Vapour Sensing Performances of Copper Oxide Nanocrystals with Mixed Phases. *Sensors Actuators, B Chem.* **2016**, *224*, 434–448. https://doi.org/10.1016/j.snb.2015.10.042.

(61) Postica, V.; Lupan, O.; Gapeeva, A.; Hansen, L.; Khaledialidusti, R.; Mishra, A. K.; Drewes, J.; Kersten, H.; Faupel, F.; Adelung, R.; Hansen, S. Improved Long-Term Stability and Reduced Humidity Effect in Gas Sensing: SiO_2 Ultra-Thin Layered ZnO Columnar Films. *Adv. Mater. Technol.* **2021**, *6* (5), 2001137. https://doi.org/10.1002/admt.202001137.

(62) Gröttrup, J.; Paulowicz, I.; Schuchardt, A.; Kaidas, V.; Kaps, S.; Lupan, O.; Adelung, R.; Mishra, Y. K. Three-Dimensional Flexible Ceramics Based on Interconnected Network of Highly Porous Pure and Metal Alloyed ZnO Tetrapods. *Ceram. Int.* **2016**, *42* (7), 8664–8676. https://doi.org/10.1016/j.ceramint.2016.02.099.

(63) Lupan, O.; Ababii, N.; Santos-Carballal, D.; Terasa, M. I.; Magariu, N.; Zappa, D.; Comini, E.; Pauporté, T.; Siebert, L.; Faupel, F.; Vahl, A.; Hansen, S.; de Leeuw, N. H.; Adelung, R. Tailoring the Selectivity of Ultralow-Power Heterojunction Gas Sensors by Noble Metal Nanoparticle Functionalization. *Nano Energy* **2021**, *88*, 106241. https://doi.org/10.1016/J.NANOEN.2021.106241.
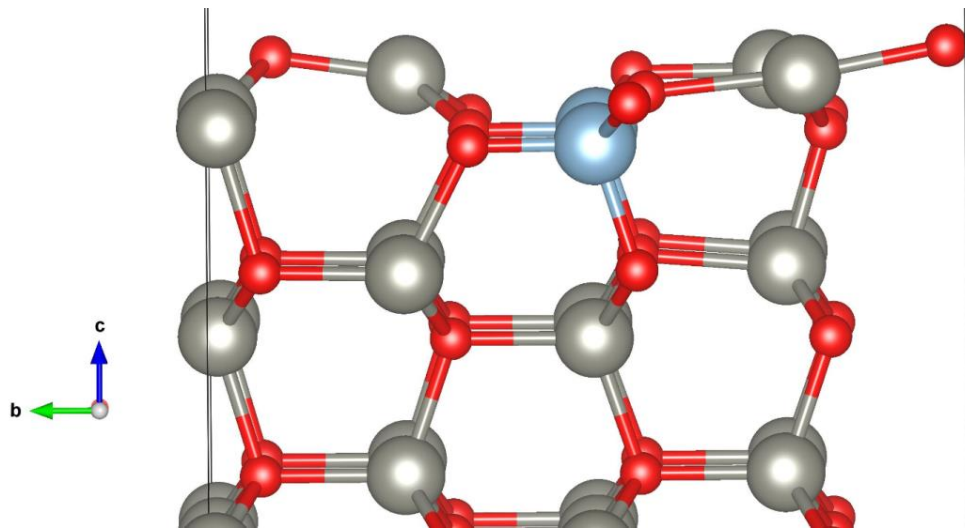
Figure 1. Relaxed structure of the Al_2O_3/ZnO $(10\bar{1}0)$ interface. Zn and O atoms are represented in grey and red colours, while blue colour indicates substituted Al atoms.

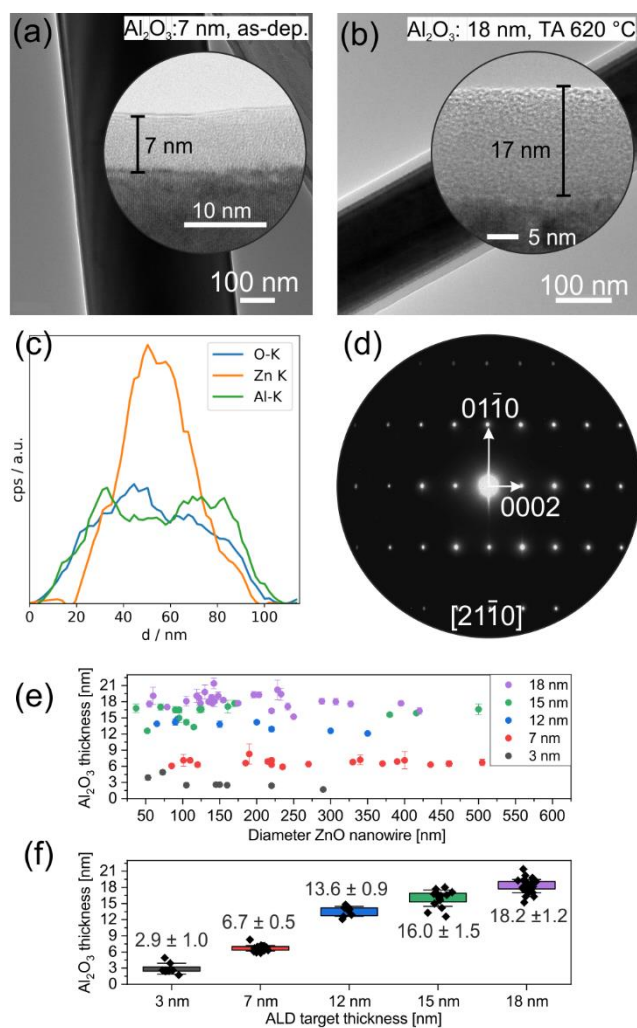**Figure 2.** (a,b) TEM images of the ZnO nanowire model systems of the Al$_2$O$_3$/ZnO heterostructures coated with 7 and 18 nm of aluminum oxide. The HRTEM micrographs show the Al$_2$O$_3$/ZnO heterostructures before (a) and after (b) annealing at 620 °C. (c) Chemical analysis by EDXS linescan across one nanowire heterostructure. (d) Electron diffraction pattern of the Al$_2$O$_3$/ZnO heterostructure showing only reflections assigned to ZnO. (e) Scatter plot of the measured coating thickness versus the ZnO diameter for various ALD processes and (f) box plots summarizing average values of Al$_2$O$_3$ thickness versus the targeted thickness.
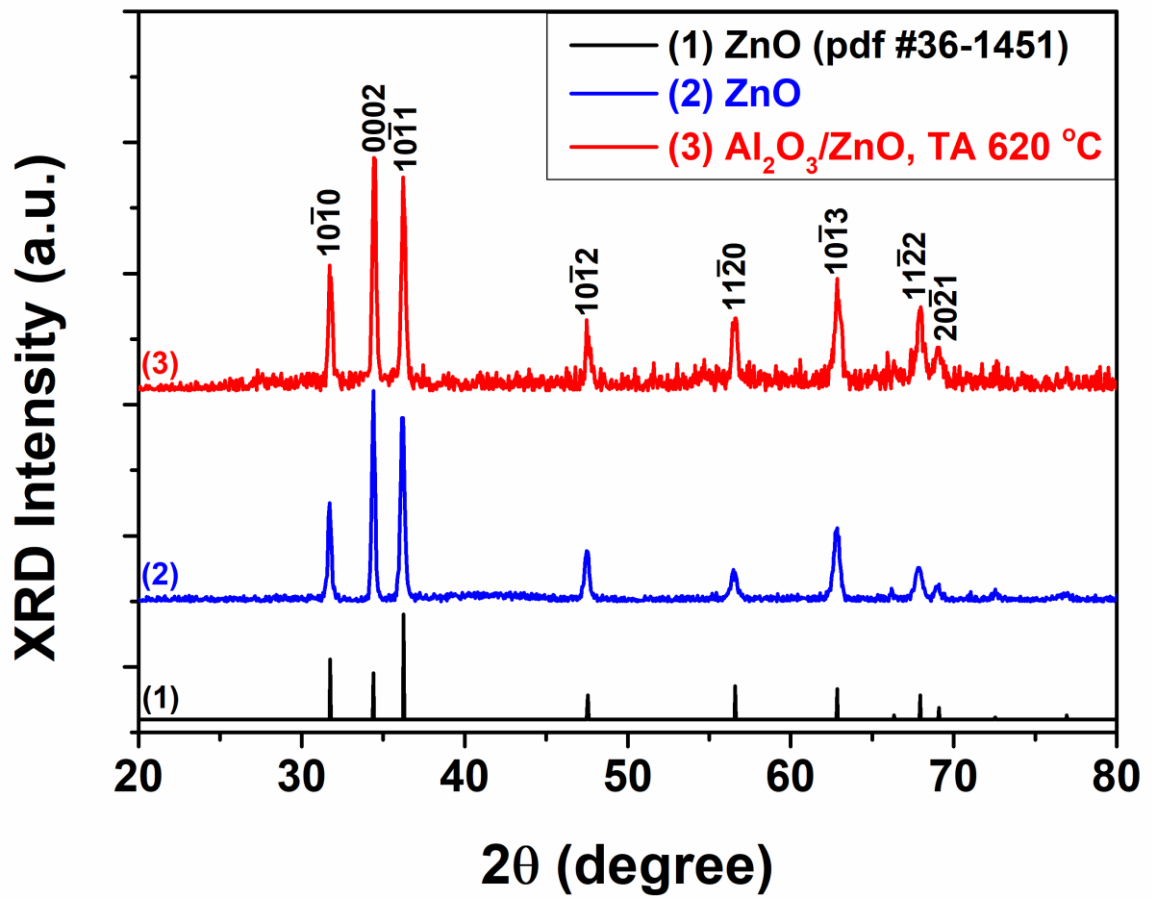
Figure 3. XRD patterns of the: ZnO based on PDF card #36-1451 (curve 1); pure ZnO (curve 2); and Al_2O_3/ZnO heterostructures containing a nano-layer of Al_2O_3 with a thickness of 15 nm (curve 3).
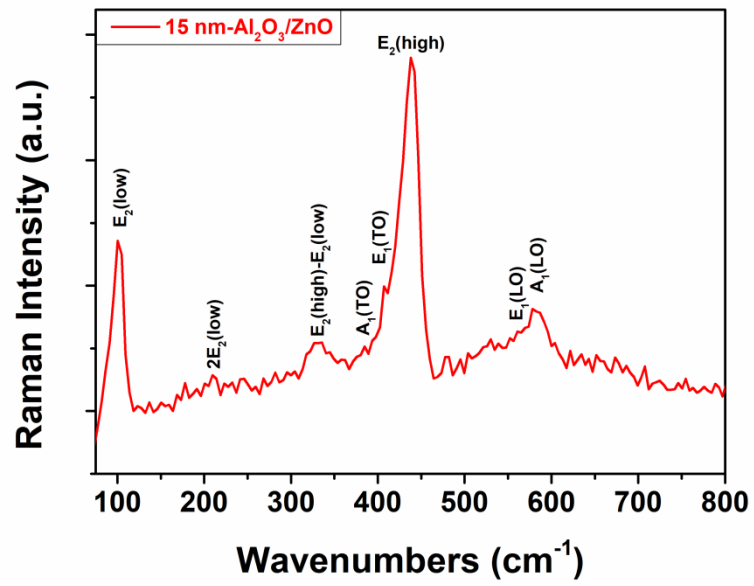
Figure 4. Room temperature micro-Raman spectrum of the annealed Al_2O_3/ZnO heterostructures containing a nano-layer of Al_2O_3 with a thickness of 15 nm.
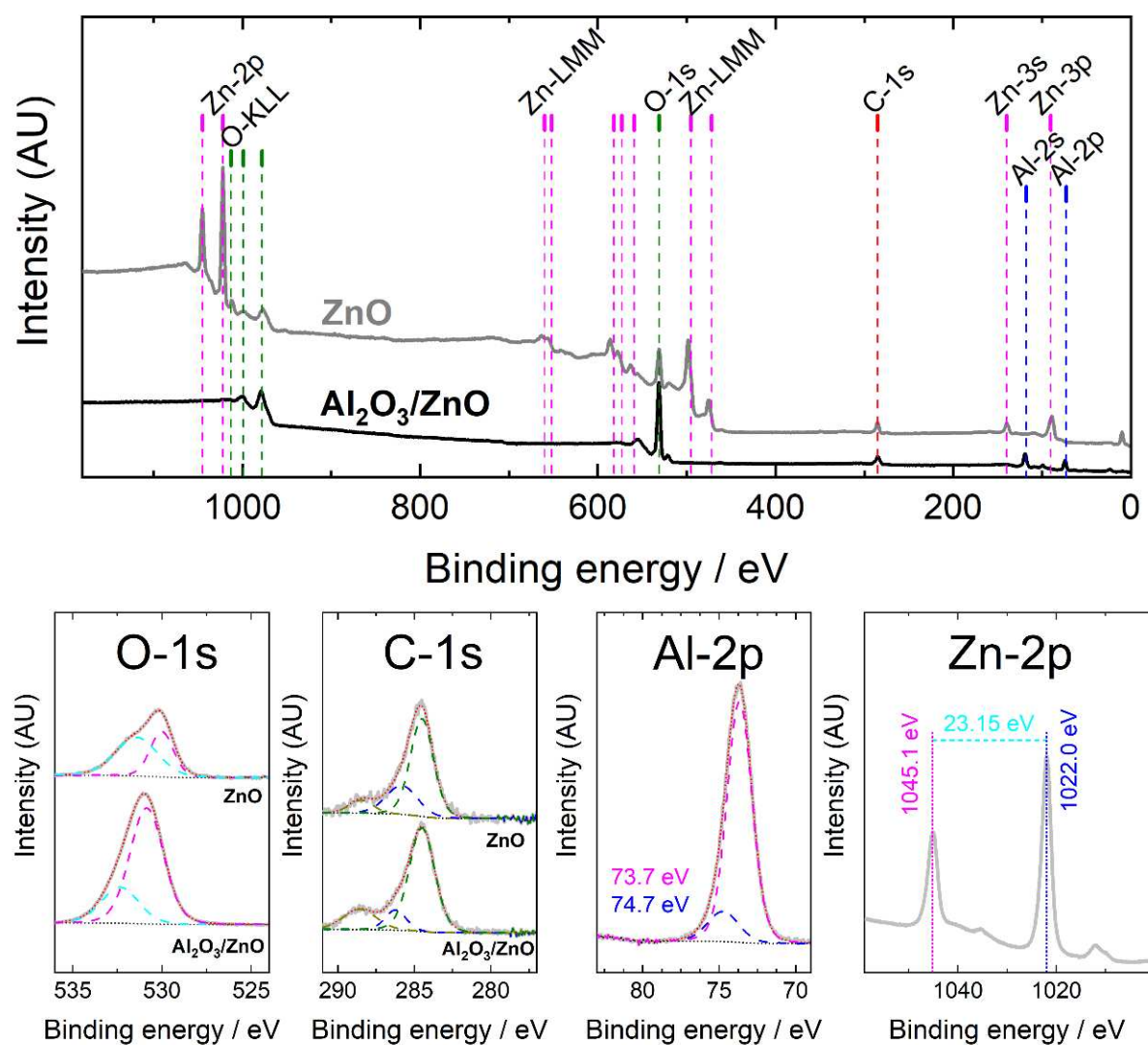
Figure 5. XPS survey (top) and high resolution (bottom) spectra of ZnO and Al_2O_3/ZnO thin films on quartz glass substrates. The presence of the elements Zn, O, C and Al is indicated by dashed lines in the survey spectrum. Deconvolution of the O-1s, C-1s and Al-2p lines is indicated by dashed lines in the high-resolution spectra.
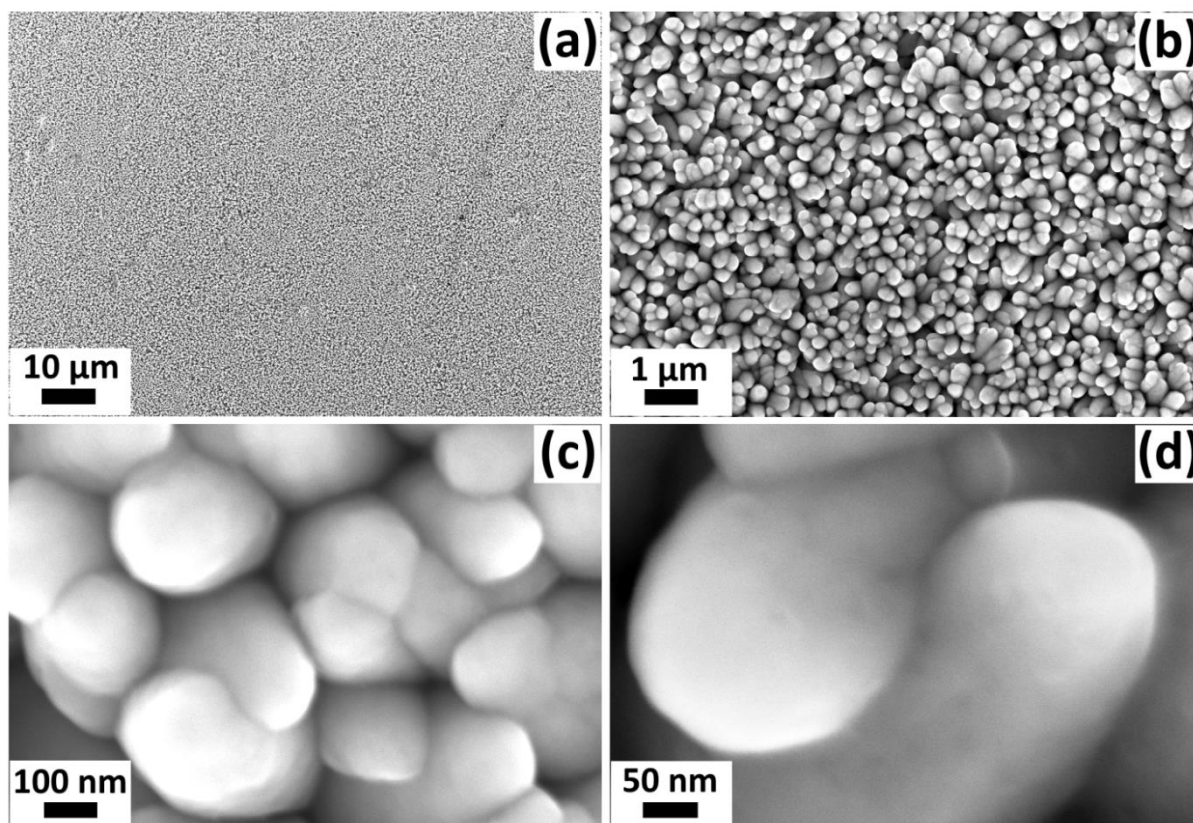
Figure 6. (a,b) low magnifications; and (c,d) high magnifications SEM images of the Al_2O_3/ZnO thin films containing a nano-layer of Al_2O_3 with a thickness of 15 nm following post-deposition thermal treatment at 620 °C for 40 min. The rough surface morphology is characterized by protruding columnar grains with large degree of mistilt from vertical growth direction and interpenetration of the grains.
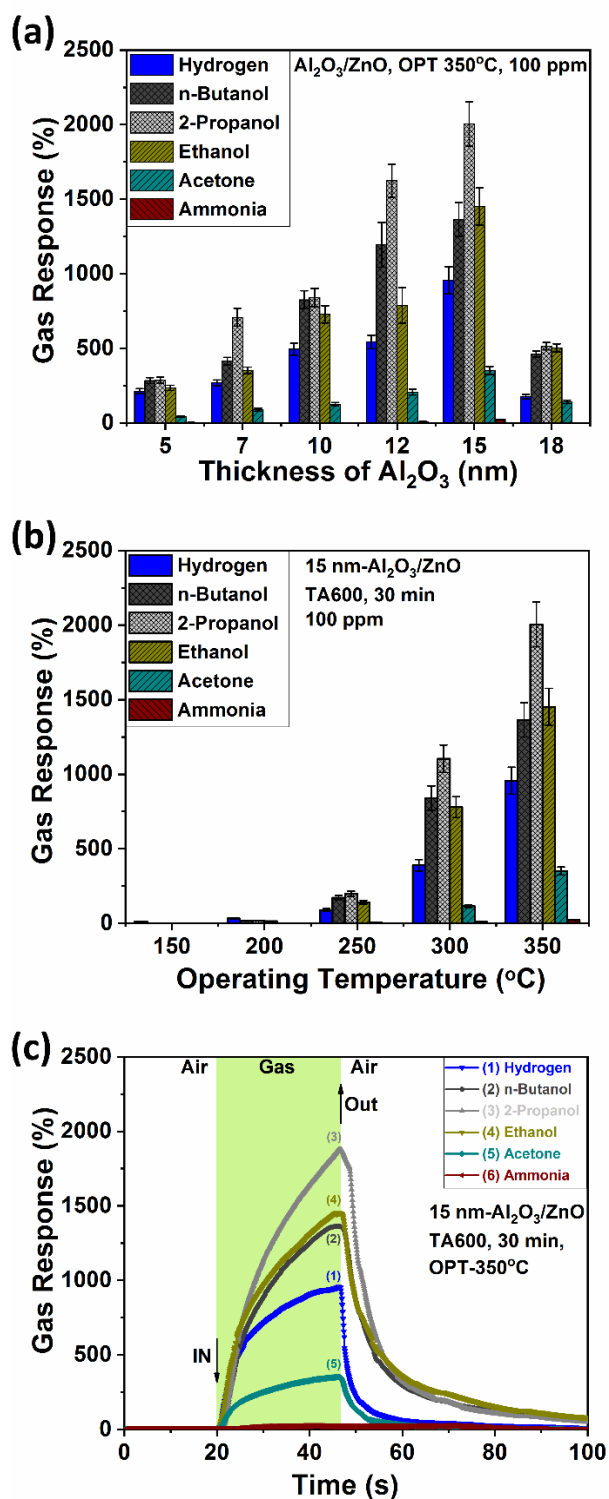
Figure 7. (a) Gas response versus thickness of Al$_2$O$_3$ overlayer (5, 7, 10, 12, 15, 18 nm). (b) Gas response versus operating temperatures, (c) Dynamic response of the Al$_2$O$_3$/ZnO sample set containing a nano-layer of Al$_2$O$_3$ with a thickness of 15 nm.

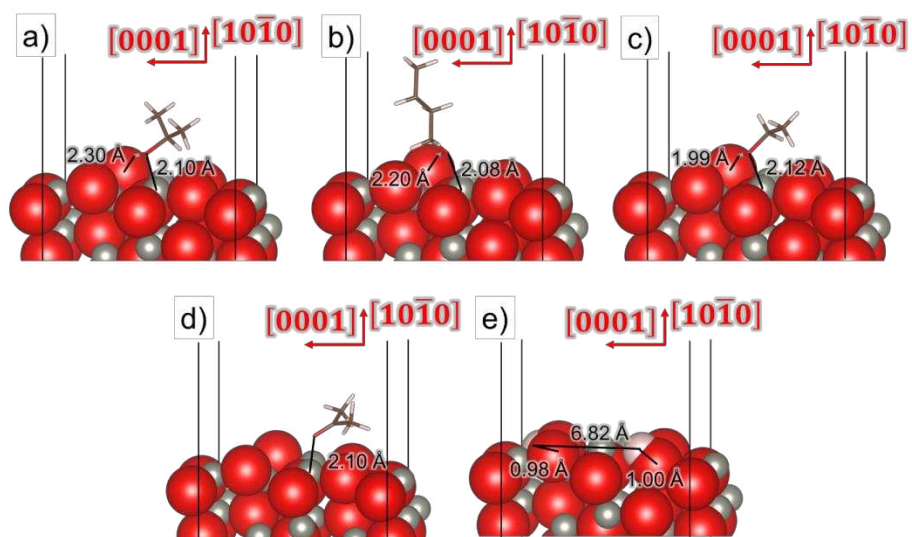**Figure 8.** Adsorption of (a) 2-C_3H_7OH, (b) n-C_4H_9OH, (c) C_2H_5OH, (d) CH_3COCH_3 and (e) H_2 on the Al_2O_3/ZnO($10\bar{1}0$) interface. Interatomic distances are indicated and crystallographic directions are shown with respect to the ZnO($10\bar{1}0$) layer. The Al_2O_3/ZnO($10\bar{1}0$) interfaces are displayed using the space-filling representation, whereas the adsorbates are indicated using the stick representation. O atoms are in red, H atoms are in white, C atoms are in brown, Zn atoms are in grey and Al atoms are in blue.
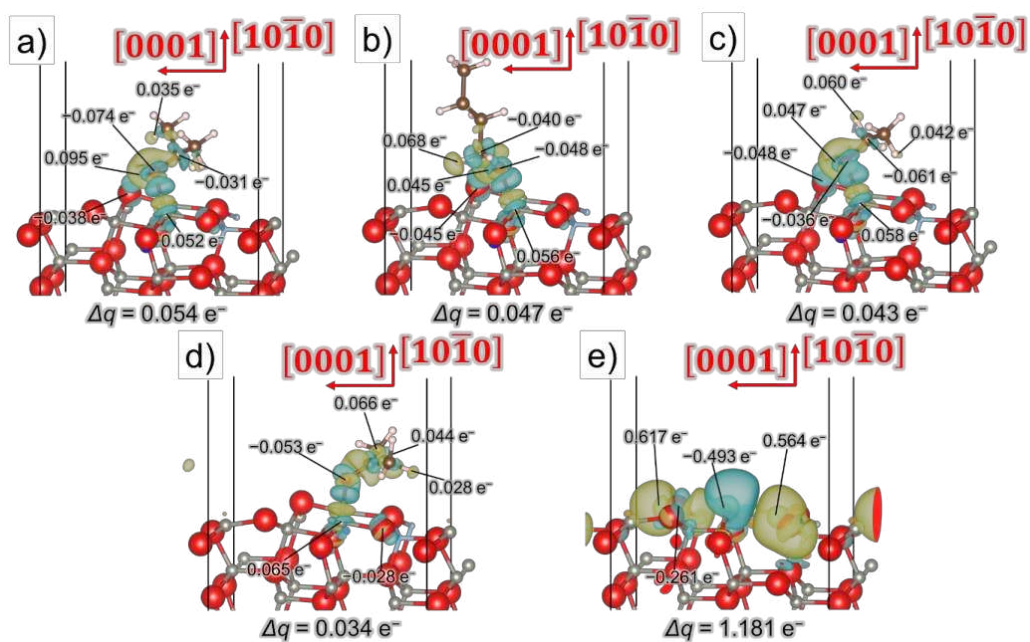
Figure 9. Charge density flow ($\Delta\rho$) for the adsorption of (a) 2-C$_3$H$_7$OH, (b) n-C$_4$H$_9$OH, (c) C$_2$H$_5$OH, (d) CH$_3$COCH$_3$ and (e) H$_2$ on the Al$_2$O$_3$/ZnO($10\bar{1}0$) interface. Crystallographic directions are indicated with respect to the ZnO($10\bar{1}0$) substrate. The Al$_2$O$_3$/ZnO($10\bar{1}0$) interfaces and the adsorbates are displayed using the ball-and-stick representation. Electron density gain and depletion surfaces are in green and yellow, respectively. Isosurfaces display a value of ±0.002 e Å^{-3}. The atomic charge density differences for the atoms that suffered the largest change are also indicated. A negative value of charge transfer denotes that the species gains electron charge. O atoms are in red, H atoms are in white, C atoms are in brown, Zn atoms are in grey and Al atoms are in blue.
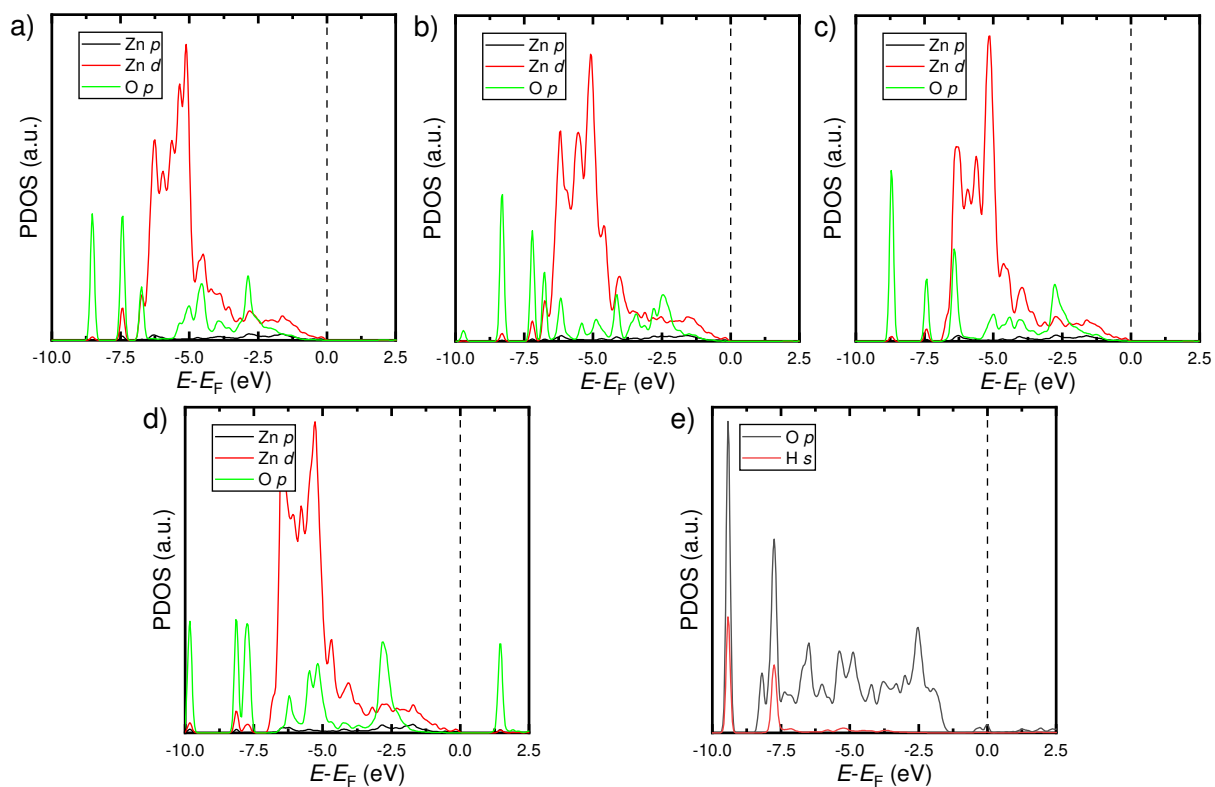
Figure 10. Atomic projections of the density of states (PDOS) for the *p* and *d* electrons of the surface Zn ions and for the *p* states of the molecular O atoms directly interacting for the most stable adsorption modes of (a) 2-C_3H_7OH, (b) *n*-C_4H_9OH, (c) C_2H_5OH and d) CH_3COCH_3 on the Al_2O_3/ZnO($10\bar{1}0$) interface. The *p* states of the surface O anions are plotted alongside the *s* orbitals of the interacting H species for the adsorption of the (e) H_2 molecule. The vertical dashed lines represent the Fermi level.

Table 1. Adsorption energies (E_{ads}) and charge transfers (Δq) for 2-C_3H_7OH, n-C_4H_9OH, C_2H_5OH, CH_3COCH_3 and H_2 on the Al_2O_3/$ZnO(10\bar{1}0)$ interface. The adsorption site of the adsorbate on the nanoparticles is also indicated. A negative value of Δq denotes that the adsorbate gains electron charge.

Adsorbate	Site	E_{ads} (eV)	Δq (e⁻)
2-C_3H_7OH	Al	−0.697	−0.019
	Zn	−1.330	0.054
n-C_4H_9OH	Al	−0.450	−0.021
	Zn	−1.329	0.047
C_2H_5OH	Al	−0.642	−0.013
	Zn	−1.245	0.043
CH_3COCH_3	Al	−0.622	−0.019
	Zn	−0.959	0.034
H_2	Molecular	−0.118	−0.011
	Dissociated	−0.434	1.181

Table 2. Adsorption energies (E_{ads}) and charge transfers (Δq) for 2-C$_3$H$_7$OH, n-C$_4$H$_9$OH, C$_2$H$_5$OH, CH$_3$COCH$_3$ as well as molecular and dissociated H$_2$ on the α-Al$_2$O$_3$(0001) and ZnO$(10\bar{1}0)$ surfaces. A negative value of Δq denotes that the adsorbate gains electron charge.

Adsorbate	α-Al$_2$O$_3$(0001)		ZnO$(10\bar{1}0)$	
	E_{ads} (eV)	Δq (e$^-$)	E_{ads} (eV)	Δq (e$^-$)
2-C$_3$H$_7$OH	−1.523	0.017	−1.126	0.041
n-C$_4$H$_9$OH	−1.501	0.011	−1.043	0.036
C$_2$H$_5$OH	−1.509	0.013	−1.071	0.033
CH$_3$COCH$_3$	−1.545	0.019	−0.926	0.044
H$_2$ molecular	−0.378	−0.197	−0.327	−0.012
H$_2$ dissociated	−0.862	1.172	−0.357	−0.018

Table of Contents.